

Using a Deep Neural Network and Transfer Learning to Bridge Scales for Seismic Phase Picking

Enter authors here: Chengping Chai¹, Monica Maceira^{1,2}, Hector J. Santos-Villalobos¹, Singanallur V. Venkatakrishnan¹, Martin Schoenball³, Weiqiang Zhu⁴, Gregory C. Beroza⁴, Clifford Thurber⁵, and EGS Collab Team

¹Oak Ridge National Laboratory, Oak Ridge, Tennessee, USA.

²Department of Physics and Astronomy, University of Tennessee, Knoxville, Tennessee, USA.

³Lawrence Berkeley National Laboratory, Berkeley, California, USA.

⁴Department of Geophysics, Stanford University, Stanford, California, USA.

⁵Department of Geology and Geophysics, University of Wisconsin-Madison, Madison, Wisconsin, USA

Corresponding author: Chengping Chai (chaic@ornl.gov)

Key Points:

- Successful transfer learning of a neural network to seismic data with orders of magnitude difference in spatial and temporal characteristics
- Created novel workflow combining deep learning and double-difference seismic imaging
- New workflow provides better seismic catalog and larger amount of phase picks compared to human analysts.

25 **Abstract**

26 The important task of tracking seismic activity requires both sensitive detection and accurate
27 earthquake location. Approximate earthquake locations can be estimated promptly and
28 automatically; however, accurate locations depend on precise seismic phase picking, which is a
29 laborious and time-consuming task. We adapted a deep neural network (DNN) phase picker
30 trained on local seismic data to meso-scale hydraulic fracturing experiments. We designed a
31 novel workflow, transfer-learning aided double-difference tomography, to overcome the three
32 orders of magnitude difference in both spatial and temporal scales between our data and data
33 used to train the original DNN. Only 3,500 seismograms (0.45% of the original DNN data) were
34 needed to re-train the original DNN model successfully. The phase picks obtained with transfer-
35 learned model are at least as accurate as the analyst's, and lead to improved event locations.
36 Moreover, the effort required for picking once the DNN is trained is a small fraction of the
37 analyst's.

38 **Plain Language Summary**

39 Seismic sensors are widely used to monitor many energy-related systems. To monitor these
40 systems effectively, we need to process a very large amount of data, which is very labor-
41 intensive. A few deep learning models have been developed to perform these tasks for
42 earthquake generated signals. We adopted one of these deep learning models developed for
43 kilometer scale and updated it for signals recorded from a meter-scale project. This process not
44 only allows us to overcome the significant spatial and temporal scale difference between our data
45 and the data used by the original deep learning model, but also significantly reduces the amount
46 of required training data. Our results show the updated model matches human performance, but
47 with a much faster speed. A workflow that combines the deep learning algorithm with existing
48 imaging technologies enables improvements for both monitoring small earthquakes and studying
49 subsurface structure.

50 **1 Introduction**

51 Seismic monitoring plays a significant role in the oil and gas industry, underground
52 mines, carbon capture and storage, and the geothermal industry due to its value for both reservoir
53 management and for risk mitigation. Valuable information, such as fracture development and
54 elastic properties of the subsurface, can be recovered from data recorded with seismic monitoring
55 systems. For example, the spatial dimensions and temporal evolution of hydraulic and/or
56 reactivated natural fractures are usually estimated by tracking seismic events. The location and
57 origin time of these microseismic events are determined by arrival times of seismic phases at
58 multiple seismic sensors. These same arrival times of primary (P) and secondary (S) waves are
59 also used for subsurface seismic imaging to measure elastic properties of the subsurface.
60 Manually picking arrival times of seismic phases is a very time-consuming task especially for
61 small-scale projects since high temporal sampling rate is required. Therefore, reliable automatic
62 phase pickers are essential for these projects. Traditional automatic pickers such as Short-Term
63 Average/Long-Term Average (STA/LTA; Allen, 1978) and Auto Regression-Akaike
64 Information Criterion (AR-AIC; Sleeman & van Eck, 1999) pickers require intensive human
65 involvement and refinement, and they do not benefit from knowledge of previous picks because
66 they treat each measurement individually. When applied to seismic data, the accuracy of
67 traditional automatic pickers may not be satisfactory, particular for noisy data. Recent
68 applications of deep-learning-based automatic seismic phase pickers (e.g. Y. Chen, 2018; Pardo

69 et al., 2019; Ross et al., 2018; Zhou et al., 2019; L. Zhu et al., 2019; W. Zhu & Beroza, 2018)
70 have shown remarkable accuracy and processing speed for seismic signals originated from
71 natural earthquakes; however, whether these deep-learning phase pickers can be used for seismic
72 monitoring remains unclear, and training such deep-learning phase pickers from scratch requires
73 a huge amount of data.

74 We use seismic data from experiment 1 of the enhanced geothermal system (EGS) Collab
75 project to test whether one of the deep-learning-based automatic phase pickers, PhaseNet (W.
76 Zhu & Beroza, 2018), is useful for mesoscale monitoring systems. The experiment was
77 conducted at the 4850-foot level of the Sanford Underground Research Facility (SURF) located
78 in Lead, South Dakota (Kneafsey et al., 2019). The testbed consists of one injection, one
79 production, and six 60 m-long monitoring boreholes. The seismic monitoring system was
80 equipped with multiple types of geophysical instruments including 24 hydrophones and 12
81 accelerometers. An 8-core workstation with an automated processing flow was deployed at the
82 experiment site. The processing scripts are capable of detecting seismic events (triggered),
83 finding initial P-wave phase picks, and inverting for initial seismic event locations and origin
84 times. Seismic event locations and origin times were improved with human reviewed and refined
85 phase picks. The original seismic catalog was processed by Schoenball et al. (2020). Several
86 hydraulic stimulations were performed since May 2018. We focused on seismic signals
87 associated with stimulations between May 22nd and December 21st of 2018. These seismic
88 signals have three orders of magnitude difference in spatial and temporal scales from the original
89 training data used by the deep learning models mentioned earlier.

90 In this paper, we directly applied the PhaseNet model (W. Zhu & Beroza, 2018) to the
91 seismic data from experiment 1 of the EGS Collab project. Although the results are reasonable,
92 we show that retraining the PhaseNet model significantly boosts performance. The process,
93 called transfer learning (TL), requires only a few thousand seismograms because the weights of
94 the DNN were trained initially by a different dataset of 0.7 million seismograms (from natural
95 earthquakes). The performance of the resulting TL model was compared with a traditional
96 automatic picker, the original PhaseNet model, and human analysts. We then applied the TL
97 model to all the seismograms from the triggered seismic events. We used the resulting TL-
98 derived phase picks and double-difference tomography (tomoDD; Zhang & Thurber, 2003,
99 2006) to constrain subsurface seismic velocities and update seismic event locations. The results
100 were compared with those using manual picks.

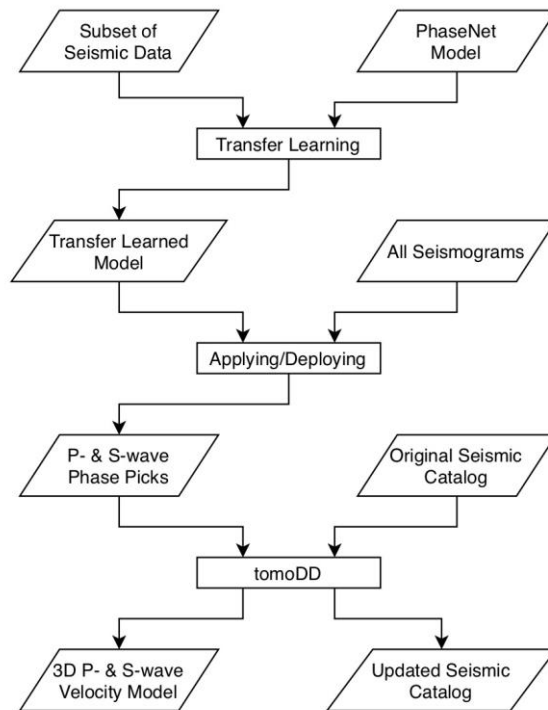
101 **2 Data**

102 Our data consist of seismograms from triggered microseismic events between May 2018
103 and December 2018 at the Experiment 1 site of the EGS Collab project, manually picked P-wave
104 and S-wave arrival times, and the original seismic catalog from (Schoenball et al., 2020). We
105 used 35 seismic sensors (one hydrophone was defective) with a 100 kHz sampling rate that were
106 deployed in six 60m-long monitoring wells (Figure S1). We detected and located the
107 microseismic events using a standard STA/LTA routine, the PhasePAPy package (C. Chen &
108 Holland, 2016), and a modified version of Hypoinverse (Klein, 2002). We cut the triggered
109 seismograms to 0.11 s long segments around the P-wave arrival times and filtered with a
110 bandpass filter between 3 kHz and 20 kHz. The filtered seismograms show clear similarity with
111 those used to train the original PhaseNet (Figure S2). We used a total of 69,444 waveform
112 segments (from 1,932 seismic events). Initial P-wave arrival times were automatically measured

113 with the PhasePAPy package. We manually reviewed and refined the P-wave arrival times. We
114 picked all S-wave arrival times manually. Additional details about the monitoring system and
115 data preprocessing procedures of the original seismic catalog can be found in (Schoenball et al.,
116 2020).

117 **3 Method**

118 We designed a workflow (Figure 1), TL-aided double-difference tomography (TADT),
119 that takes advantage of two existing technologies, deep neural networks (DNN) and seismic
120 double-difference tomography. We started with the pre-trained DNN model, PhaseNet (W. Zhu
121 & Beroza, 2018), that was trained with over 0.7 million seismic recordings from in and around
122 northern California for natural earthquakes. The PhaseNet model was trained using 30 s long
123 seismograms sampled at 100 Hz. The earthquake-station distance for these data is on the order of
124 10's of kilometers. Our monitoring system for our data samples at 100 kHz and the source-sensor
125 distance is on the order of 10 meters. Despite the three orders of magnitude differences in both
126 sampling rate and source-sensor distance between the PhaseNet data and our data, we found that
127 PhaseNet produced acceptable results when applied to our data. To improve the performance
128 further, we updated the PhaseNet model with a subset of seismic data that meets the training data
129 requirements (three-component seismograms with both P- and S-wave picks) for PhaseNet. We
130 then applied the resulting TL model to all the triggered seismograms (30 ms long) to obtain TL
131 derived P- and S-wave phase picks. We used the tomoDD package (Zhang & Thurber, 2003,
132 2006) to update the seismic catalog and simultaneously image the subsurface tomographically.
133 The TADT workflow allows us to reduce the human effort significantly.



134

135 **Figure 1.** A flowchart of TL-aided seismic tomography using PhaseNet (W. Zhu & Beroza,
 136 2018) and tomoDD (Zhang & Thurber, 2003, 2006).

137

138 3.1 Transfer learning

139 During the TL process, we use the same network architecture as PhaseNet and initialize
 140 the weights with the PhaseNet model. We visually inspected the selected seismograms and
 141 excluded 343 (9%) incorrect phase picks. The remaining 3,478 seismograms belong to 1,872
 142 distinct seismic events. The total number of seismograms we used is only 0.45% of that used by
 143 the original PhaseNet. We randomly divided the seismic events into training, validation, and test
 144 sets. The training set (2,443 waveforms) was used to retrain the DNN model, the validation set
 145 (345 waveforms) was used to select the optimal model from different training runs, and the test
 146 set (690 waveforms) was used to evaluate performance (Figure S3). Similar to W. Zhu & Beroza
 147 (2018), we used a Gaussian distribution with a standard derivation of 0.1 ms centered on the
 148 manual picks to represent manual pick uncertainty. We allowed the entire neural network to
 149 change during TL, and used the Adam optimizer (Kingma & Ba, 2014). We used a learning rate
 150 (determines the step size of each iteration) of 0.01 and a batch size (number of training samples
 151 used each time) of 20. Our tests indicate using filtered data leads to better performance than raw
 152 data. We applied a bandpass filter with corner frequencies of 3 kHz and 20 kHz to the
 153 seismograms before feeding them into the neural network for training, which is different from
 154 W. Zhu & Beroza (2018). For a fair comparison, the bandpass filter was applied to all the
 155 seismograms throughout this study.

156 3.2 Double-difference tomography

157 The original seismic catalog was processed with a homogeneous seismic velocity model
158 (Schoenball et al., 2019). Here we used the double-difference tomography package tomoDD
159 (Zhang & Thurber, 2003, 2006) to simultaneously minimize the uncertainty in seismic event
160 locations due to spatial seismic velocity variations and to constrain the 3D subsurface P-wave
161 and S-wave velocity model for the seismically active region. Since the tomoDD package was
162 originally designed for kilometer-scale problems, we made some modifications (e.g. input and
163 output format, coordinate system) specifically for meter-scale projects. We estimated both P- and
164 S-wave seismic velocity models. We relocated 1,743 seismic events and discretized a 3D volume
165 of 77 m (easting), 83 m (northing), and 40 m (vertical) with nodes 1 m apart in each direction
166 (then interpolated to 0.1 m by the tomoDD package). The initial model was homogeneous with a
167 P-wave speed of 5.9 km/s and an S-wave speed of 3.5 km/s. These two velocities were obtained
168 from curve fitting of travel-time observations (travel-time versus distance). Numerous previous
169 studies (e.g. Chai et al., 2019; Syracuse et al., 2016) have shown that appropriate inversion
170 parameters are required for a well-constrained seismic velocity model. We used an L-curve
171 analysis (similar to Hansen, 1992) to find the optimal set of inversion parameters. An optimal
172 weight of 10 was used for smoothing and 200 for damping (see Zhang & Thurber, 2003 for
173 definition). We obtained the final velocity models and updated seismic catalog after eight
174 iterations. The final models fit the observations better than the starting homogeneous model
175 (Figure S4 and S5).

176 4 Results

177 Our results are new phase picks, updated seismic event locations, and 3D seismic
178 velocity models. Hyper Text Markup Language (HTML) based interactive visualizations (similar
179 to Chai et al., 2018) were used to inspect seismic event locations and seismic velocity models.

180 4.1 Phase picks

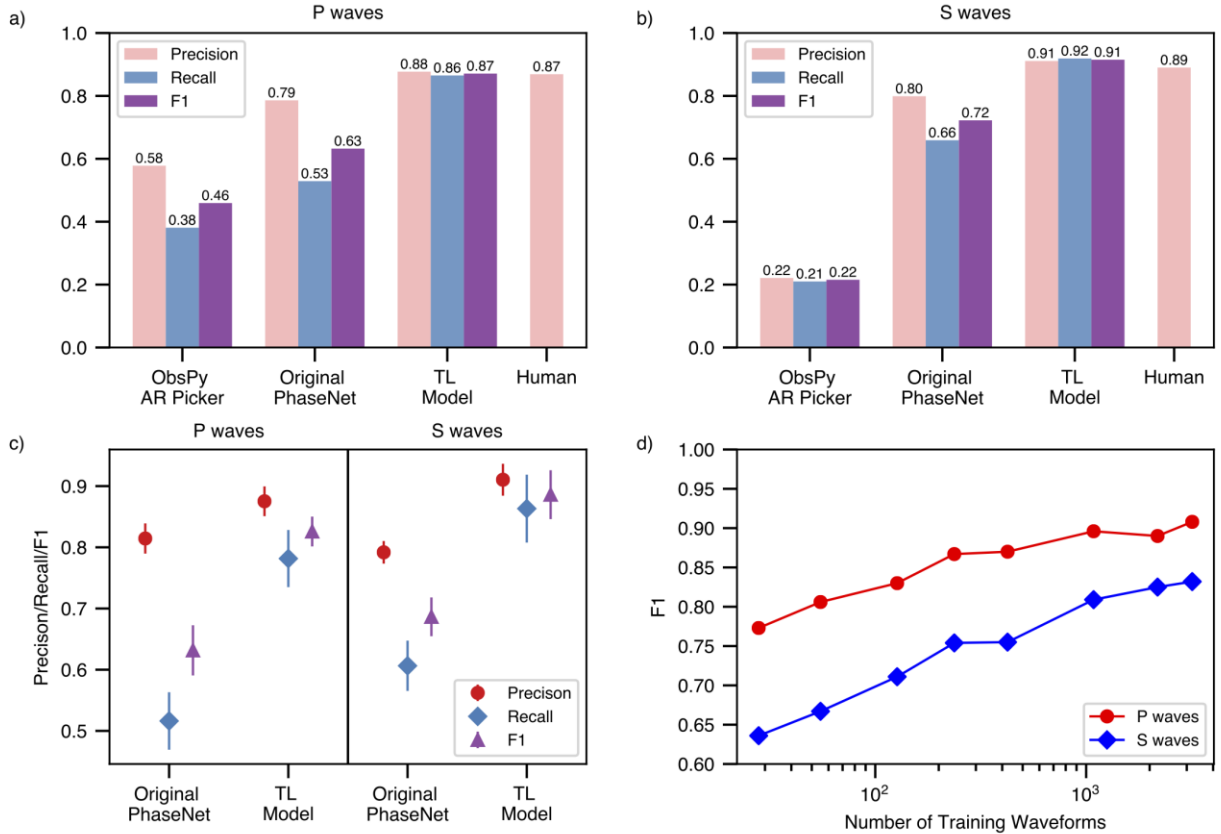
181 The TL model we obtained measures phase picks from seismograms with high accuracy.
182 Some randomly selected waveforms and associated phase picks from the test dataset are shown
183 in Figure S6. We can see that the TL results agree with manual picks even when the background
184 noise level is high. Inspecting the data when TL results differ from manual picks, we noticed that
185 the TL model is able to correct some human errors or skip difficult-to-pick signals (more often
186 for P-waves than for S-waves). The difference between TL results and manual picks is just
187 slightly larger than the threshold (0.1 milliseconds), for many cases in Figure S6. The TL model
188 is more prone to error when signals are very complex.

189 We compared the TL results with those using the Obspy (Beyreuther et al., 2010)
190 implementation of an AR picker (Akazawa, 2004), the original PhaseNet, and human analysts
191 (Figure 2). We use precision, recall, and F1 score (see Text S1 for definition) to quantify and
192 compare the performance. We estimated the performance of human analysts by having three
193 analysts manually pick the phase arrival times from the same 100 three-component seismograms
194 (to reduce time cost). For each seismogram, we considered the median of the three manual picks
195 as the ground truth. We also measured the human performance for each analyst by comparing
196 results from each analyst against the ground truth. The human performance in Figure 2a and 3b
197 was the average of the three analysts. The original PhaseNet produced much better results than
198 the AR picker for both P and S waves. The TL model outperformed the original PhaseNet with

199 an improvement of roughly 0.1 in precision and 0.3 in recall, highlighting the importance of re-
200 training the DNN with our data. The TL model is the only one among the three automatic pickers
201 that has a performance comparable to human analysts. The TL model performed slightly better
202 on S waves than human analysts, which could be due to the larger SNRs compared to P waves.
203 The TL model achieved human performance in a fraction of the time.

204 We used a 5-fold cross-validation to measure the uncertainties in the performance
205 matrices. We divided all the available waveforms (including training, validation, and test set)
206 into five folds (equal parts). Five TL models were trained using one of the five combinations of
207 four folds for each training and validated with the other fold. The performance of these five TL
208 models was used to compute the uncertainty of the performance. The performance improvement
209 is larger than the measurement uncertainty (Figure 2c). We also trained TL models with different
210 number of training waveforms and tested the TL models with the same test dataset. As expected,
211 F1 scores of the TL models for both P and S waves improve as more training data were included
212 (Figure 2d).

213 When we apply the TL model to all the triggered seismograms, the TL model finds more
214 S-wave picks than the human expert. We performed 3D double-difference tomography using
215 manual picks and TL derived picks with the same inversion parameters. Although fewer P-wave
216 picks were obtained by the TL model compared to the human analyst, the updated seismic
217 locations using TL-derived picks show a more compact distribution compared to that using
218 manual picks (see the next section for details). Specifically, we found 18,543 acceptable P-wave
219 picks and 8,935 S-wave picks from the human expert using a total of 69,444 seismograms. The
220 TL model identified 12,050 acceptable P-wave picks (20% of which were included in the
221 training dataset) and 13,297 S-wave picks (18% of which were included in training dataset).



222

223 **Figure 2.** A comparison of performance between human (three analysts), the ObsPy AR picker,
 224 the original PhaseNet, and the TL model for (a) P waves and (b) S waves. The human
 225 performance was measured with a smaller data set (100 waveforms) due to cost. (c) shows
 226 uncertainty (2 sigma) of the performance matrices for the original PhaseNet model and the TL
 227 model measured with a 5-fold cross-validation. (d) shows the F1 score as a function of the
 228 number of training waveforms used for TL.

229

4.2 Updated seismic locations

230

231

232

233

234

235

236

237

238

239

240

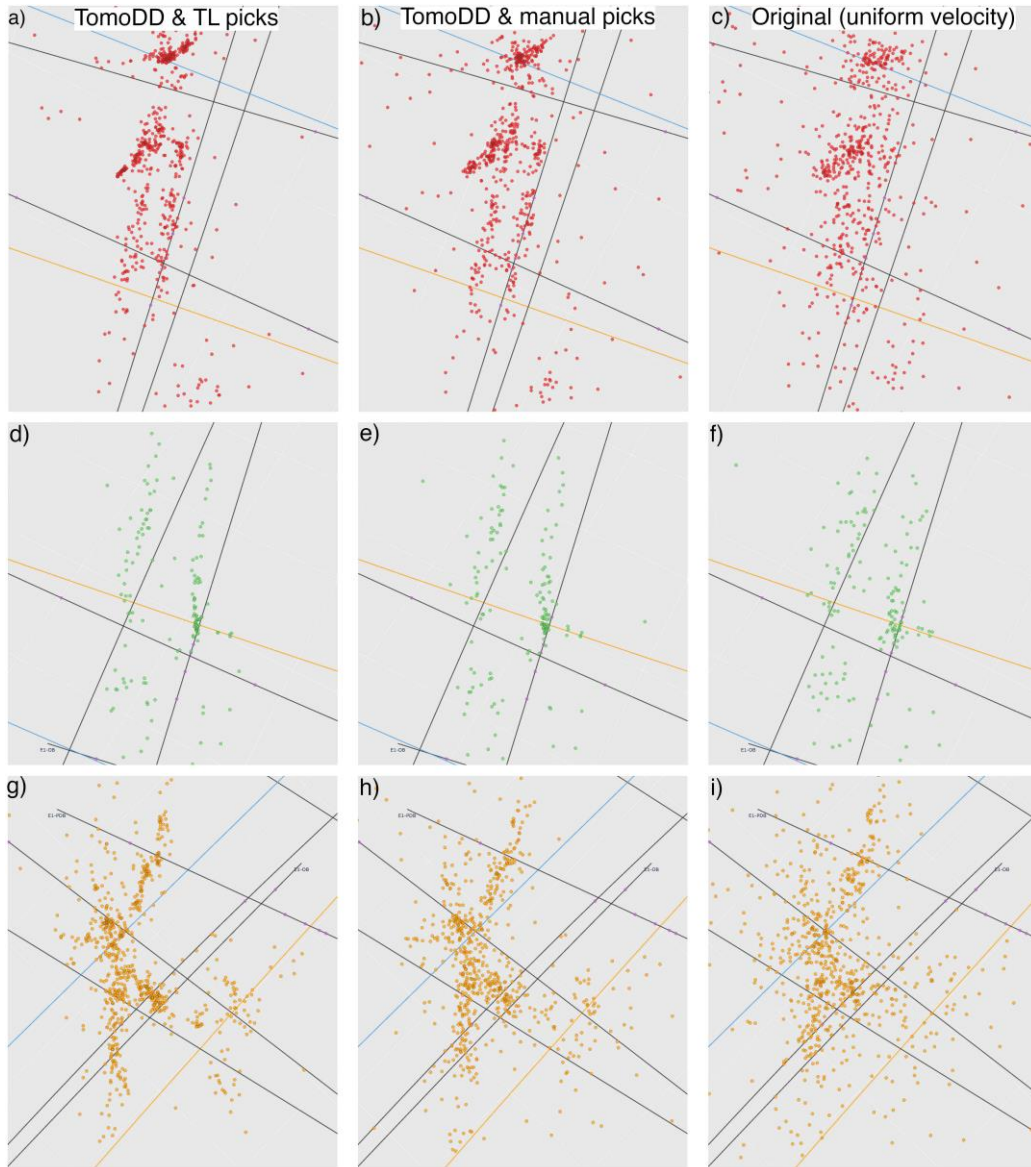
241

242

243

We examine seismic locations associated with the May 2018 stimulations (May 22-25), June 2018 stimulation (June 25), and December 2018 stimulations (December 21 & 22) in Figure 3. Details of these stimulations can be found in Schoenball et al. (2020). Compared to the original seismic locations, the updated locations from double-difference tomography using either manual picks or the TL-derived picks show more detailed geometry of the fractures. For the May 2018 stimulations (Figure 3a-c), the updated seismic locations show two parallel fractures that are not obvious in the original locations. Since these two fractures intercepted one monitoring borehole, we were able to confirm these fractures with independent temperature data recorded in the borehole using distributed temperature sensing with 0.25 m spatial resolution (Fu et al., 2020). Using the TL-derived picks leads to more tightly clustered seismic locations. For the June 2018 stimulation (Figure 3d-f), both the original and updated seismic locations show two fractures. Compared to the original, the updated locations show a slightly tighter pattern delineating the activated fractures. For the December 2018 stimulations (Figure 3g-i), the original locations show two intersecting fractures, but the geometry of these fractures was not

244 well constrained, especially near the two ends of the fractures. When we relocated the seismic
 245 event locations using the manual picks, these two fractures showed a tighter pattern. When TL-
 246 derived picks were used for relocation, these two fractures were constrained even better and we
 247 can see the two ends of the fractures more clearly. As indicated by the updated seismic event
 248 locations, the TL-derived picks are equivalent to or better than the manual picks in imaging the
 249 activated fractures.



250

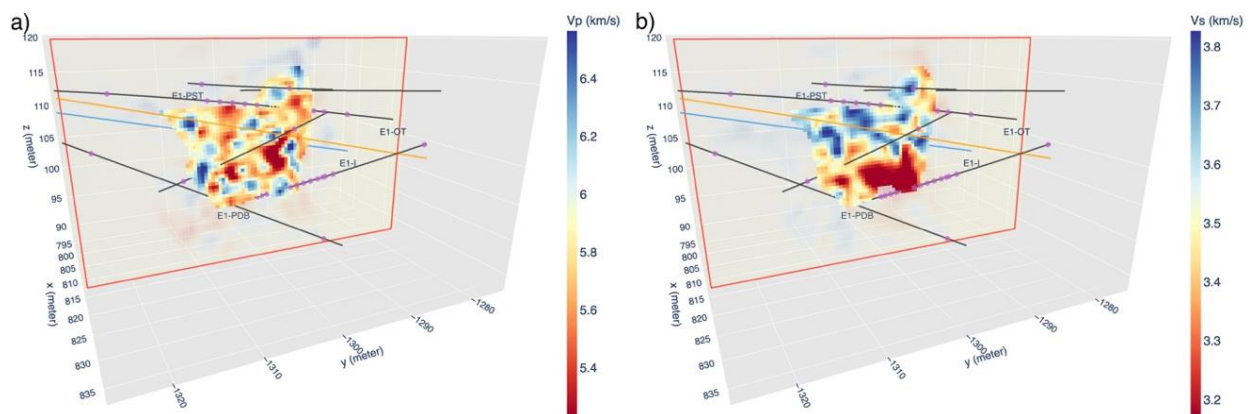
251 **Figure 3.** A comparison of original (c, f, and i) and updated (a, b, d, e, g, and h) microseismic
 252 event locations associated with stimulations in May 2018 (a, b, and c), June 2018 (d, e, and f),
 253 and December 2018 (g, h, and i). Seismic events in the left panel (a, d, and g) show locations
 254 updated with TL-derived phase picks using tomoDD. The middle panel (b, e, and h) shows
 255 locations updated with manual picks using tomoDD. Fractures are clearly visible with TL-
 256 derived phase picks. The lines are boreholes.

257

258 4.3 3D seismic velocity model

259 We constrained both P-wave and S-wave seismic velocities with double-difference
 260 tomography. The P-wave velocity model shows significant spatial heterogeneity when either
 261 manual picks or TL-derived picks were used in the tomographic inversion. Slices of the 3D P-
 262 wave and S-wave velocity models obtained using TL-derived picks are shown in Figure 4. The
 263 P-wave velocity model contains some small-scale high-velocity anomalies. To first order, the P-
 264 wave velocity is lower at a greater depth. The S-wave velocity model shows a smoother pattern
 265 with a low-velocity zone imaged at an elevation below 105 meters. The average P-wave velocity
 266 agrees with that obtained from active source surveys (Schoenball et al., 2020).

267 To identify the volume that we can reliably image, we performed checkerboard tests
 268 using data simulated according to both manual picks and TL-derived picks. For the checkerboard
 269 tests, we started with an artificial model with alternating high and low velocities. Synthetic P-
 270 wave and S-wave phase picks were computed using the artificial model matching the actual
 271 observations between seismic event and seismic sensor pairs. The synthetic phase picks were
 272 then used in tomography with a uniform starting model. The recovered (inverted) model is
 273 compared to the true model to identify the volume that is well-constrained by the data. To
 274 measure the volume, we first compute the absolute difference between the recovered model and
 275 the true model at each grid cell. A grid cell is considered well-constrained when the recovered
 276 seismic velocities are less than 0.1 km/s away for P waves or 0.06 km/s for S waves from the
 277 ground truth. The well-constrained volume is smoothed by applying a 3D spatial Gaussian filter
 278 with a standard derivation of 1 m in each direction to all of the well-constrained grid cells. Slices
 279 of the recovered P- and S-wave velocity models using manual picks and TL-derived picks are
 280 shown in Figure S7 and S8. For the P-wave velocity model, the well-constrained volume is 2,678
 281 m³ for manual picks and 2,465 m³ (8% decrease) for TL-derived picks. For the S-wave velocity
 282 model, the well-constrained volume is 815 m³ for manual picks and 1,895 m³ (133% increase)
 283 for TL-derived picks.



284
 285 **Figure 4.** The final (a) P- and (b) S-wave velocity models inverted using TL picks. The lines are
 286 boreholes. The dots represent seismic sensors.

287 **5 Discussion and Conclusions**

288 We present a workflow that integrates TL and seismic double-difference tomography. As
 289 demonstrated with the EGS Collab data, the workflow can produce better seismic event

290 locations, improve subsurface imaging capabilities, and reduce the overall time cost compared to
291 the original labor-intensive workflow. Our results also show that the TL model obtained by
292 retraining the PhaseNet DNN leads to human-level performance despite the significant
293 differences in the study area size, sensor geometry, and sampling rate between the data used to
294 develop and train PhaseNet and our data. Other types of geophysical observations such as P-
295 wave receiver functions, surface-wave measurements, and gravity observations (e.g. Chai et al.,
296 2015; Maceira & Ammon, 2009; Syracuse et al., 2016) can be inverted together with TL-derived
297 phase picks when data are available.

298 Since phase picks are the basis for both locating seismic events and imaging the
299 subsurface, it is valuable to determine seismic phase picks quickly and reliably. The PhaseNet
300 model leads to better picks than many traditional auto-pickers such as the ObsPy implementation
301 of the AR picker (W. Zhu & Beroza, 2018). A TL model initialized with the PhaseNet model and
302 retrained with only around 3,600 three-component seismograms and associated manual picks
303 outperforms the original PhaseNet model by over 10% in terms of precision and recall. The TL
304 model performs equally to or slightly better than a human expert. The TL model found fewer
305 (32%) P-wave picks but more (48%) S-wave picks than the human expert. Since the double-
306 difference tomography results that used these TL-derived phase picks show better seismic event
307 locations compared to those using manual picks, it is likely the TL model removed low-quality
308 P-wave picks and added high-quality S-wave picks. The speed of the TL model (or PhaseNet) is
309 about 1,900 times (excluded training time) faster than the human expert. Weights of the TL
310 model show first-order similarities and small differences compared to the PhaseNet model
311 (Figure S9-S11). A comparison (Figure S12 and S13) of convolutional features of hidden layers
312 for an example input using the PhaseNet model and the TL model suggests that these small
313 changes lead to better hidden features (more impulsive peaks).

314 Double-difference tomography tests using manual picks and TL derived picks show that
315 the latter lead to better seismic event locations and a larger (133% increase) well-constrained
316 volume for the S-wave velocity model. Even though we obtained fewer P-wave picks with the
317 TL model compared to the human expert, the well-constrained volume for the P-wave velocity
318 model only decreased slightly. The improved seismic event locations allow us to see detailed
319 structures of the fracture planes, which in turn will help us better constrain the fracture geometry.
320 Two parallel fracture planes were confirmed with independent borehole observations (Fu et al.,
321 2020).

322 Our results show that we can reduce the time cost significantly, and improve results, by
323 adding TL into the proposed workflow. Seismic phase picking is labor intensive and thus
324 expensive. It took on the order of several days to determine all the seismic phase picks from the
325 69,444 seismograms recorded. For the presented workflow, the analyst would only need to
326 manually pick around 3,500 high-quality seismograms. Retraining the PhaseNet model took
327 around one hour (using 32 2.1 GHz Intel Xeon cores). Processing all the seismograms with the
328 TL model took only nine minutes on a laptop computer (with six 2.9 GHz Intel i9 cores). Even
329 including the retraining time, the presented workflow takes much less time than human labor.
330 The speed can be increased with greater computational power. Moreover, the TL model can be
331 directly used on future seismic data from the same recording system without retraining. The
332 proposed workflow is an economical way to monitor subsurface fracture evolution and image
333 subsurface seismic structure with high resolution. The workflow is also applicable to new study
334 areas.

335 **Acknowledgments and Data**

336 This material was based upon work supported by the U.S. Department of Energy, Office
 337 of Energy Efficiency and Renewable Energy (EERE), Office of Technology Development,
 338 Geothermal Technologies Office, under Award Number DE-AC05-00OR22725. The United
 339 States Government retains, and the publisher, by accepting the article for publication,
 340 acknowledges that the United States Government retains a non-exclusive, paid-up, irrevocable,
 341 world-wide license to publish or reproduce the published form of this manuscript, or allow others
 342 to do so, for United States Government purposes. The research supporting this work took place
 343 in whole or in part at the Sanford Underground Research Facility in Lead, South Dakota. The
 344 assistance of the Sanford Underground Research Facility and its personnel in providing physical
 345 access and general logistical and technical support is acknowledged. We thank Haijiang Zhang
 346 for sharing the tomoDD package. We thank Yarom Polsky, Amir Ziabari and Derek Rose for
 347 helpful discussions. We acknowledge comments and suggestions from Jacob Hinkle, Jeffrey
 348 Johnson, and Philip Bingham. The authors declare that there is no conflict of interest regarding
 349 the publication of this article. The views and conclusions contained in this document are those of
 350 the authors and should not be interpreted as necessarily representing the official policies, either
 351 expressed or implied, of the U.S. Government.

352 Seismograms and initial microseismic catalog can be downloaded at
 353 <https://gdr.openei.org/submissions/1166> (last accessed in February 2020). Final microseismic
 354 catalog, seismic velocity models, and associated visualizations are available at
 355 <http://gdr.openei.org/submissions/1214> (last accessed in April 2020). Matplotlib (Hunter, 2007)
 356 and plotly (<https://plot.ly>, last accessed in March 2020) were used to generate figures. Some
 357 calculations were performed with Numpy (van der Walt et al., 2011). The original PhaseNet
 358 model can be accessed at <https://github.com/wayneweiqiang/PhaseNet> (las accessed in March
 359 2020).

360 **References**

- 361 Akazawa, T. (2004). A technique for automatic detection of onset time of P-and S-Phases in
 362 strong motion records. In *13th World Conference on Earthquake Engineering* (p. 786).
- 363 Allen, R. V. (1978). Automatic earthquake recognition and timing from single traces. *Bulletin of*
 364 *the Seismological Society of America*, 68(5), 1521–1532.
- 365 Beyreuther, M., Barsch, R., Krischer, L., Megies, T., Behr, Y., & Wassermann, J. (2010). ObsPy:
 366 A Python Toolbox for Seismology. *Seismological Research Letters*, 81(3), 530–533.
 367 <https://doi.org/10.1785/gssrl.81.3.530>
- 368 Chai, C., Ammon, C. J., Maceira, M., & Herrmann, R. B. (2015). Inverting interpolated receiver
 369 functions with surface wave dispersion and gravity: Application to the western U.S. and
 370 adjacent Canada and Mexico. *Geophysical Research Letters*, 42(11), 4359–4366.
 371 <https://doi.org/10.1002/2015GL063733>
- 372 Chai, C., Ammon, C. J., Maceira, M., & Herrmann, R. B. (2018). Interactive Visualization of
 373 Complex Seismic Data and Models Using Bokeh. *Seismological Research Letters*, 89(2A),
 374 668–676. <https://doi.org/10.1785/0220170132>
- 375 Chai, C., Maceira, M., Santos-Villalobos, H., & Team, E. C. (2019). Subsurface Seismic
 376 Structure Around the Sanford Underground Research Facility. In *44th Workshop on*

- 377 *Geothermal Reservoir Engineering* (pp. 1364–1376).
- 378 Chen, C., & Holland, A. A. (2016). PhasePapy: A Robust Pure Python Package for Automatic
 379 Identification of Seismic Phases. *Seismological Research Letters*, 87(6), 1384–1396.
 380 <https://doi.org/10.1785/0220160019>
- 381 Chen, Y. (2018). Automatic microseismic event picking via unsupervised machine learning.
 382 *Geophysical Journal International*, 212(1), 88–102. <https://doi.org/10.1093/gji/ggx420>
- 383 Fu, P., Wu, H., Ju, X., & Morris, J. (2020). Analyzing Fracture Flow Channel Area in EGS
 384 Collab Experiment 1 Testbed. In *45th Workshop on Geothermal Reservoir Engineering* (pp.
 385 1283–1292).
- 386 Hansen, P. C. (1992). Analysis of Discrete Ill-Posed Problems by Means of the L-Curve. *SIAM*
 387 *Review*, 34(4), 561–580. <https://doi.org/10.1137/1034115>
- 388 Hunter, J. D. (2007). Matplotlib: A 2D Graphics Environment. *Computing in Science &*
 389 *Engineering*, 9(3), 90–95. <https://doi.org/10.1109/MCSE.2007.55>
- 390 Kingma, D. P., & Ba, J. (2014). Adam: A Method for Stochastic Optimization. *3rd International*
 391 *Conference on Learning Representations, ICLR 2015 - Conference Track Proceedings*.
 392 Retrieved from <http://arxiv.org/abs/1412.6980>
- 393 Klein, F. W. (2002). User’s Guide to HYPOINVERSE-2000, a Fortran Program to Solve for
 394 Earthquake Locations and Magnitudes. *U.S. Geol. Surv. Open File Report 02-171*.
 395 <https://doi.org/http://geopubs.wr.usgs.gov/open-file/of02-171/>
- 396 Kneafsey, T. J., Blankenship, D., Knox, H. A., Johnson, T. C., Ajo-Franklin, J. B., Schwering, P.
 397 C., et al. (2019). EGS Collab Project: Status and Progress. In *44th Workshop on Geothermal*
 398 *Reservoir Engineering* (pp. 1335–1350).
- 399 Maceira, M., & Ammon, C. J. (2009). Joint inversion of surface wave velocity and gravity
 400 observations and its application to central Asian basins shear velocity structure. *Journal of*
 401 *Geophysical Research*, 114(B2), B02314. <https://doi.org/10.1029/2007JB005157>
- 402 Pardo, E., Garfias, C., & Malpica, N. (2019). Seismic Phase Picking Using Convolutional
 403 Networks. *IEEE Transactions on Geoscience and Remote Sensing*, 57(9), 7086–7092.
 404 <https://doi.org/10.1109/TGRS.2019.2911402>
- 405 Ross, Z. E., Meier, M.-A., & Hauksson, E. (2018). P Wave Arrival Picking and First-Motion
 406 Polarity Determination With Deep Learning. *Journal of Geophysical Research: Solid Earth*,
 407 123(6), 5120–5129. <https://doi.org/10.1029/2017JB015251>
- 408 Schoenball, M., Ajo-Franklin, J., Blankenship, D., Cook, P., Dobson, P., Guglielmi, Y., et al.
 409 (2019). Microseismic monitoring of meso-scale stimulations for the DOE EGS Collab
 410 project at the Sanford Underground Research Facility. In *44th Workshop on Geothermal*
 411 *Reservoir Engineering* (pp. 1392–1399).
- 412 Schoenball, M., Ajo-franklin, J. B., Blankenship, D., Chai, C., Dobson, P., Kneafsey, T., et al.
 413 (2020). Creation of a mixed-mode fracture network at meso-scale through hydraulic
 414 fracturing and shear stimulation. <https://doi.org/10.1002/essoar.10502549.1>
- 415 Sleeman, R., & van Eck, T. (1999). Robust automatic P-phase picking: an on-line
 416 implementation in the analysis of broadband seismogram recordings. *Physics of the Earth*

- 417 *and Planetary Interiors*, 113(1–4), 265–275. [https://doi.org/10.1016/S0031-9201\(99\)00007-](https://doi.org/10.1016/S0031-9201(99)00007-2)
418 2
- 419 Syracuse, E. M., Maceira, M., Prieto, G. A., Zhang, H., & Ammon, C. J. (2016). Multiple plates
420 subducting beneath Colombia, as illuminated by seismicity and velocity from the joint
421 inversion of seismic and gravity data. *Earth and Planetary Science Letters*, 444, 139–149.
422 <https://doi.org/10.1016/j.epsl.2016.03.050>
- 423 van der Walt, S., Colbert, S. C., & Varoquaux, G. (2011). The NumPy Array: A Structure for
424 Efficient Numerical Computation. *Computing in Science & Engineering*, 13(2), 22–30.
425 <https://doi.org/10.1109/MCSE.2011.37>
- 426 Zhang, H., & Thurber, C. (2003). Double-Difference Tomography: The Method and Its
427 Application to the Hayward Fault, California. *Bulletin of the Seismological Society of*
428 *America*, 93(5), 1875–1889. <https://doi.org/10.1785/0120020190>
- 429 Zhang, H., & Thurber, C. (2006). Development and Applications of Double-difference Seismic
430 Tomography. *Pure and Applied Geophysics*, 163(2–3), 373–403.
431 <https://doi.org/10.1007/s00024-005-0021-y>
- 432 Zhou, Y., Yue, H., Zhou, S., & Kong, Q. (2019). Hybrid event detection and phase-picking
433 algorithm using convolutional and recurrent neural networks. *Seismological Research*
434 *Letters*, 90(3), 1079–1087. <https://doi.org/10.1785/0220180319>
- 435 Zhu, L., Peng, Z., McClellan, J., Li, C., Yao, D., Li, Z., & Fang, L. (2019). Deep learning for
436 seismic phase detection and picking in the aftershock zone of 2008 M7.9 Wenchuan
437 Earthquake. *Physics of the Earth and Planetary Interiors*, 293(May 2018), 106261.
438 <https://doi.org/10.1016/j.pepi.2019.05.004>
- 439 Zhu, W., & Beroza, G. C. (2018). PhaseNet: A Deep-Neural-Network-Based Seismic Arrival
440 Time Picking Method. *Geophysical Journal International*, 216(1), 261–273.
441 <https://doi.org/10.1093/gji/ggy423>

442

443 **Appendix**

444 EGS Collab Team includes J. Ajo-Franklin, T. Baumgartner, K. Beckers, D.
445 Blankenship, A. Bonneville, L. Boyd, S. Brown, J.A. Burghardt, C. Chai, Y. Chen, B. Chi, K.
446 Condon, P.J. Cook, D. Crandall, P.F. Dobson, T. Doe, C.A. Doughty, D. Elsworth, J. Feldman,
447 Z. Feng, A. Foris, L.P. Frash, Z. Frone, P. Fu, K. Gao, A. Ghassemi, Y. Guglielmi, B. Haimson,
448 A. Hawkins, J. Heise, C. Hopp, M. Horn, R.N. Horne, J. Horner, M. Hu, H. Huang, L. Huang,
449 K.J. Im, M. Ingraham, E. Jafarov, R.S. Jayne, S.E. Johnson, T.C. Johnson, B. Johnston, K. Kim,
450 D.K. King, T. Kneafsey, H. Knox, J. Knox, D. Kumar, M. Lee, K. Li, Z. Li, M. Maceira, P.
451 Mackey, N. Makedonska, E. Mattson, M.W. McClure, J. McLennan, C. Medler, R.J. Mellors, E.
452 Metcalfe, J. Moore, C.E. Morency, J.P. Morris, T. Myers, S. Nakagawa, G. Neupane, G.
453 Newman, A. Nieto, C.M. Oldenburg, T. Paronish, R. Pawar, P. Petrov, B. Pietzyk, R. Podgorney,
454 Y. Polsky, J. Pope, S. Porse, J.C. Primo, C. Reimers, B.Q. Roberts, M. Robertson, W.
455 Roggenthen, J. Rutqvist, D. Rynders, M. Schoenball, P. Schwering, V. Sesetty, C.S. Sherman, A.
456 Singh, M.M. Smith, H. Sone, E.L. Sonnenthal, F.A. Soom, P. Sprinkle, C.E. Strickland, J. Su, D.
457 Templeton, J.N. Thomle, V.R. Tribaldos, C. Ulrich, N. Uzunlar, A. Vachaparampil, C.A.
458 Valladao, W. Vandermeer, G. Vandine, D. Vardiman, V.R. Vermeul, J.L. Wagoner, H.F. Wang,

459 J. Weers, N. Welch, J. White, M.D. White, P. Winterfeld, T. Wood, S. Workman, H. Wu, Y.S.
460 Wu, E.C. Yildirim, Y. Zhang, Y.Q. Zhang, Q. Zhou, and M.D. Zoback.
461